Charge Accumulation Kinetics in Multi-redox Molecular Catalysts Immobilised on TiO_2

Supporting Information

All potentials are expressed *versus* NHE.

Materials and methods

The molecular catalysts used in this work, **CoP[1]** (ref.[1, 2]), **CoP[2]** (ref.[3, 4]) and **CotpyP** (ref. [5, 6]), were synthesised and characterised as reported previously. All the chemicals, including acetonitrile anhydrous 99.8% (ACN), triethanolamine 99% (TEOA) and tetrabutylammonium hexafluorophosphate 98% ($TBAPF_6$), were purchased from Sigma Aldrich. Fluorine-doped tin oxide (FTO)-coated glass sheets (SnO_2/F, 7Ωsq^{-1} sheet resistance, 300 × 300 × 2 mm) and ITO nanopowder (diameter < 50 nm; BET = 27 m^2 g^{-1} ; 90% In_2O_3, 10% SnO_2) were also purchased from Sigma Aldrich.

TiO_2 Film Preparation

A paste with 15 nm anatase TiO_2 nanoparticles was prepared from a sol-gel colloidal suspension containing 12.5 wt% TiO_2 particles and 6.2 wt% Carbowax 20000, which was prepared using the same reagents and procedure as in ref. [7, 8]. Films were then prepared by doctor-blading the paste on clean FTO on glass, drying for ~20 min. and sintering at 450 ˚C degrees for 30 min. The glass-FTO substrate was previously cleaned by washing with soap, distilled water and isopropanol and heating at 450 ˚C degrees for 30 min. The resulting films had a thickness of ~4 μm, 10-50 nm diameter pores, a porosity of 50±5%, a BET surface area per gram (S_g) of 106 m^2/g, and a roughness factor (surface area divided by projected area) around 450.[8-10]

ITO Film Preparation

FTO-coated glass was cleaned by immersing it in a solution of H_2O/37% NH_3/30% H_2O_2 (50:17:33 v/v) at 80 °C for 15 min. The electrodes were rinsed with water and successive sonication in ethanol and acetone for 15 minutes each, followed by drying at 70 °C in air before further use. A dispersion of 20% weight ITO nanoparticles was prepared in 5 M acetic acid in ethanol solution. After sonication for 30 minutes in an ice-cooled sonication bath, the ITO thin films were spin-coated onto the cleaned FTO-glass substrates. The electrodes were finally sintered at 450 °C for 30 minutes. The electrodes had a geometrical area of approximately 0.25 cm^2.

Film loading with catalyst

The TiO_2 films were prepared just before loading the catalyst; otherwise, they were heated to 450 ˚C for 30 min prior to the loading. The molecular catalysts **CoP[1]** and **CoP[2]** were loaded on TiO_2 by

soaking ~1 cm^2 films on 1x2 cm^2 FTO-glass in 5 mL MeOH:H_2O 1:1 with ~0.1 mM of catalyst for 12 h. **CotpyP** was loaded by soaking the TiO_2 films in 5 mL MeOH with 0.25 mM of catalyst for 12 h. Three films were soaked in each solution. Once loaded, all the films were rinsed first with methanol and then with acetonitrile and were left to dry in the air for at least 12h before they were used. The spectroscopic features of the catalyst were observed to remain constant in methanol for at least 48 h, more than 4 times the timespan of all the experiments. The amount of loaded catalyst was determined by measuring the absorption differences in the soaking solution.

Spectro(electro)chemistry

A three-electrode cell consisting of a platinum counter electrode and a Ag/AgCl reference electrode saturated with KCl was used for all the spectroelectrochemical and time-resolved measurements under bias. The potential of ferrocene (Fc) *versus* the Ag/AgCl sat. KCl electrode was calculated in ACN 0.1M $TBAPF_6$ to be $E_{1/2}(Fc^+/Fc)$ = 0.55 V, where the half-wave potential was calculated as an average between the potentials of the oxidative and the reductive peaks.[11, 12] Taking into account a difference of +0.63 V between Fc and NHE,[13] potentials *versus* NHE were calculated from the potentials *versus* Ag/AgCl sat. KCl by subtracting −0.08 V to ($E_{NHE}=E_{Ag/AgCl\ sat.\ KCl}$ −0.08 V). A *Metrohm Autolab PGSTAT101* potentiostat was used together with an *Agilent Technologies Cary 60* UV-Vis spectrophotometer. The absorption spectra were measured under argon purging after applying a constant potential to the sample until the current had stabilised (after ~5 min.). Every spectrum was measured at least three times to check its reproducibility.

The absorption coefficients of the catalysts in MeOH and MeOH:ACN (1:1) were determined by measuring the absorption of 4 solutions of MeOH with a known concentration of catalyst. Following the Lambert-Beer law, the amount of catalyst loaded on TiO_2 was calculated from the difference in the absorption of the catalyst solution before and after the films had been immersed in it; the loading was calculated as an average between 10 samples. The absorption coefficients of reduced species of **CoP^2** were deduced from the spectro(electro)chemistry results of ITO-**CoP^2**, where the concentration of catalyst was determined as on TiO_2. The experimental errors were calculated by following conventional error propagation equations, and by considering standard deviations of the different identical measurements or regression errors.

Theoretical Calculations

Fully optimised molecular structures were obtained through geometry optimisations employing the B3LYP[14-16] or TPSSh[17-21] functional in conjunction with the def2-TZVP[22, 23] or the 6-31G(d,p)[24-26] basis set. In such computations that were conducted on Br-containing molecules with 6-31G(d,p) as the basis set, Br was described by def2-tzvp. All calculations were conducted with ORCA 4.0.1.2[27] Solvation was approximated by the conductor-like screening model COSMO[28] with the permittivity set to ACN. Long range Coulomb and HF exchange interactions were included using the rijcosx approximation. Dispersion correction was conducted using the Grimme atom-pairwise correction with Becke-Johnson damping scheme (d3bj).[29, 30] Single point energy and frequency calculations were carried out on the optimised structures. All plots of computed structures were produced with Avogadro 1.1.0.[31] TD-DFT calculations were carried out with ORCA 4.0.1.2 on geometry optimised structures using the same basis set as for the respective geometry optimisation. The structure and absorption spectra of all the intermediates considered here are provided below.

Time-resolved spectroscopy

In time-resolved absorption spectroscopy, a 355-nm laser beam produced with an Nd:YAG crystal coupled to an optical parametric oscillator (*Opotek Opolette 355*) was used as a pump to excite the TiO_2, while the probe light was generated by a 100 W *Bentham* tungsten lamp. The wavelength of the probe beam was selected with two *Horiba Scientific OBB* monochromators placed before and after the sample. A suitable long-pass filter regulated by a *FW101C Thorlabs* mechanical colour wheel and a 400-nm long-pass filter were additionally placed after the sample. The probe light was detected by a *Hamamatsu S3071* silicon PIN photodiode, and processed by a *Costronics 2004* optical transient amplifier, a *Tektronix DPO 3012* digital phosphor oscilloscope and a *National Instruments X Series Multifunction* DAQ. Unless otherwise stated, all the results shown are the average of 16 measurements consisting of one 7-ns 355-nm pulse each irradiated with 0.8 Hz pulse frequency (referred to as 'repetition rate') through the film. Irradiation through the glass or through the film showed the same trends; when the samples were irradiated through the glass, however, the signals were weaker due to absorption by the substrate. All measurements were done under argon after 15 minutes equilibration purging with argon and keeping the light pump on. The transient photocurrent (TPC) signal in Figure S3 was obtained by measuring the potential difference between the sample and the counter electrode across a 98.7 Ohm resistor under an applied bias of −0.08 V *vs.* NHE, using a platinum counter electrode and a saturated Ag/AgCl reference electrode. Because the TPC signal is measured as a transient potential difference, TPC signals could not be obtained for the samples investigated without an applied bias. The potential of the working electrode was monitored with a voltammeter *versus* the potential of the saturated Ag/AgCl reference electrode. Spectra after 5 s irradiation were measured by exciting TiO_2 with a 365-nm LED pulse. Every measurement was repeated at least three times within every experiment to check the stability of the signal.

The measurement of transient absorption spectra took typically around 2 h. During 2 h, under applied bias (-0.08V *vs.* NHE) under high light excitation (~1.4 mJ/cm^2), the characteristic signal of the CoP^2 multi-reduced species at 700 nm was observed to decrease by ≤13%. This slight decrease of the signal at 700 nm was interpreted as catalyst degradation or detachment from the electrode and, to minimise this, the samples were always replaced after 2 h.

Photochemistry

A purpose-built liquid/solid Teflon-lined reactor setup was assembled. A solid Teflon filler was inserted into the Teflon vessel to occupy 50 % of the vessel volume. The TiO_2-CoP^2 films on FTO glass were fixed horizontally on the top surface of the Teflon filler, with the TiO_2-CoP^2 films on the top. The vessel was filled with 22 mL of the electrolyte mixture containing ACN:H_2O in 9:1 v/v ratio, 0.1 M $TBAPF_6$, and 0.1 M TEOA aqueous solution. The vessel was inserted in a closed stainless steel reactor. Zero grade (99.998%) N_2 gas was bubbled through a solution of acetonitrile at controlled rates using mass flow controllers (Omega Engineering, 0 to 100 mL min^{-1}). The system was purged with N_2 gas bubbled through ACN for 30 min to ensure that purge gas flux was saturated with acetonitrile to prevent evaporation of the electrolyte. The photoreactor was vacuumed and replenished with N_2 five times. A Xe arc lamp (300 W, $\lambda > 325$ nm, LOT Quantum Design), equipped with a water filter was used as the irradiation source, irradiating the samples through the TiO_2 surface where the catalyst was loaded. The total lamp intensity at the sample was 1750 W/m^2 between 315 and 900 nm (455 W/m^2 at 314-500 nm). Under semibatch operation, the reactor was pressurised up to 1.28 bar, with the evolved gases sampled after 5 hours of irradiation. The evolved gases were detected using a gas chromatograph (Agilent Technologies, 7890B), which was equipped with hayesep (Agilent J&W 6 foot, 1/8 inch, 2 mm, HayeSep Q Column 80/100 SST) and molecular sieve (Agilent J&W 6 foot, 1/8 inch, 2 mm, MolSieve 5A, 60/80, preconditioned) packed columns in series.

Quantum efficiency calculations

In TiO_2-**CoP²**, assuming that the 700-nm TAS signal is only due to Co(RR) formed from Co(R) and electrons in the conduction band of TiO_2, the quantum yield of accumulative electron transfer to the catalyst at the point of maximum absorption change is:

$$\frac{moles\ of\ Co(RR)\ formed}{moles\ of\ incident\ photons} = \frac{\Delta A_{700nm} - \Delta A_{700nm,\ -0.08\ V,1.16\ mJ/cm^2.}}{\varepsilon_{Co(RR)} - \varepsilon_{Co(R)}} \Big/ \frac{E_{pulse}}{h\frac{c}{\lambda}} N \qquad (1)$$

Where $\Delta A_{700nm,max.}$ is the absorption change at 700 nm 10 ms after excitation; $\Delta A_{700nm,-0.08V,\ 1.16mJ/cm2}$ is the absorption change baseline due to electrons at 700 nm 10 ms after excitation with a 1.16 mJ/cm² pulse under −0.08 V *vs.* NHE; $\varepsilon_{Co(I)}$ and $\varepsilon_{Co(II)}$ are the absorption coefficients of Co^{I} and Co^{II} respectively; E_{pulse} is the energy per laser pulse; h is the Planck constant; c is the speed of light; λ is the excitation wavelength; and N is the Avogadro number.

In TiO_2-**CotpyP**, the optical signals and the absorption coefficients considered in the calculation of the quantum efficiency (equation 1) correspond to $\lambda = 550\ nm$ and $t = 12\ \mu s$. In this case, because the signal is assigned to a double reduction ($Co^{III} \rightarrow Co(RR)$), the quantum efficiency is multiplied by 2 (two moles of photons is needed per each mole of Co(RR)).

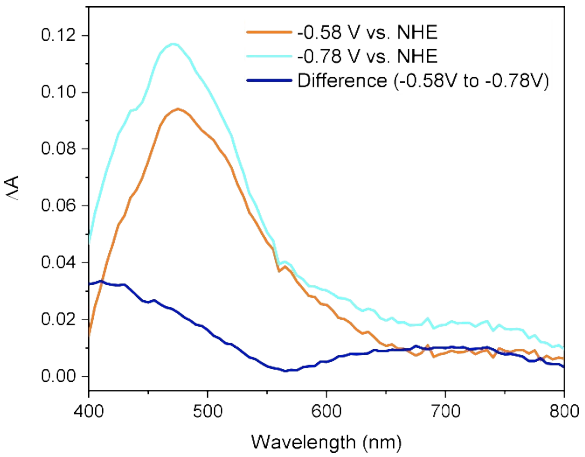

Figure S0. Absorption of TiO_2-**CoP²** at -0.58 V and -0.78 V *vs.* NHE with respect to -0.08 V, and the difference between the two. This data is shown normalised in Figure S1A.

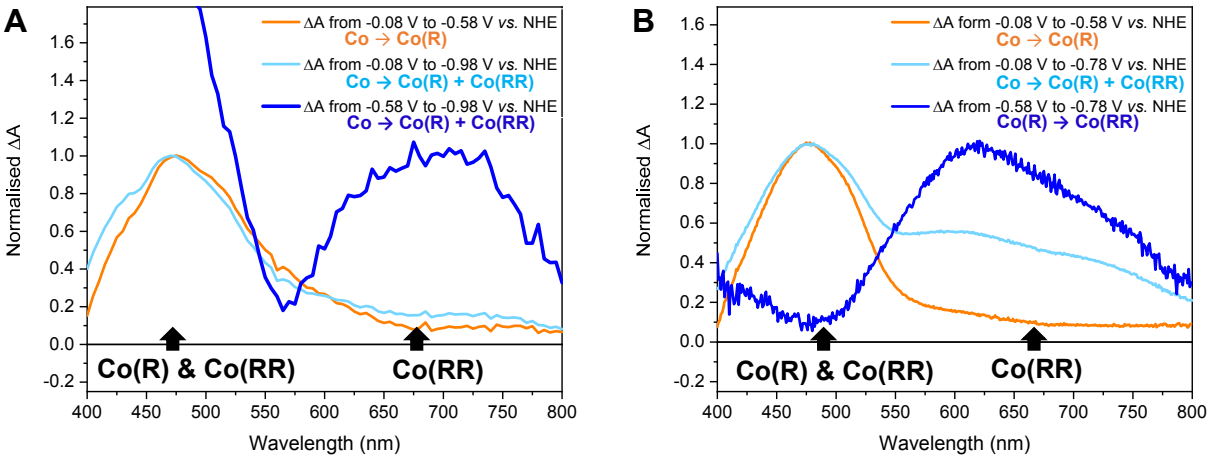

Figure S1. Steady state absorption changes of **(A)** TiO_2-**CoP²** and **(B)** ITO-**CoP²** in ACN 0.1 M $TBAPF_6$. Co(R) and Co(RR) stand for mono- and multi- reduced catalyst species respectively. Two main absorption features are observed when reductive potentials are applied to a **CoP²**-loaded electrode: at ~480 nm and at 650-700 nm. The first one (~450-500 nm) is formed at higher potentials and it is assigned to the first one-electron reduction of **CoP²** to yield Co(R). The second absorption signal (600-700 nm) appears at more negative (or reducing) potentials and it is assigned to the subsequent reduction of Co(R) to Co(RR). The approximate spectra of each of these reduced species can be obtained by subtracting the absorption spectra at two different potentials: the potential where the less reducing species is formed and the more reducing potential where the species of interest is reduced. Following the TD-DFT calculations herein, the slight differences between the signals on ITO vs. TiO_2 at 600-700 nm are probably due to differences in the trace amount of water and the hydrophilicity of the samples, in addition to possible electrostatic effect, as described in the main text.

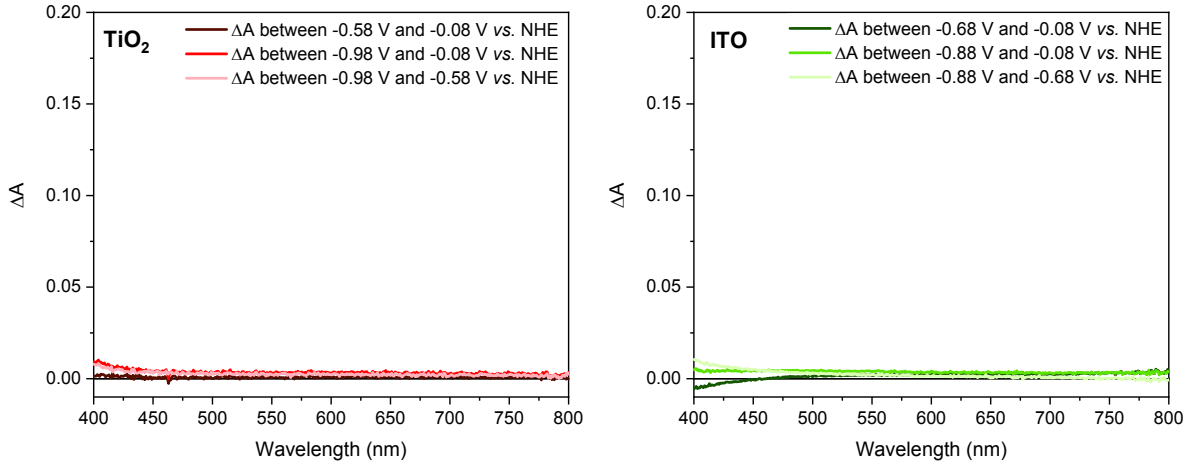

Figure S2. Steady state absorption changes of **(A)** TiO_2 and **(B)** ITO in ACN 0.1 M $TBAPF_6$. The scale of the y-axis is similar to that of Figure 2B to facilitate the comparison.

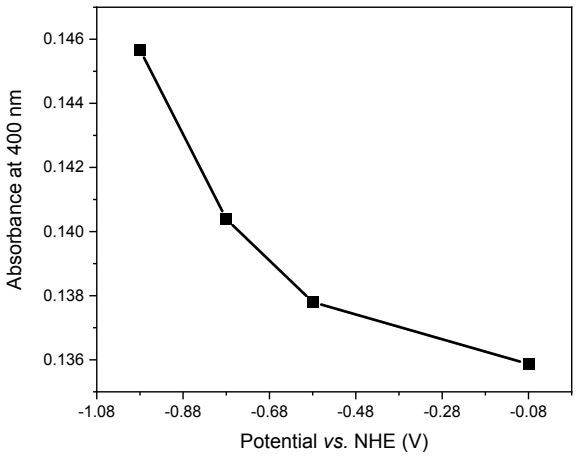

Figure S3. Potential dependence of the absorbance at 400 nm in a 4-µm mesoporous TiO_2 film, prepared as detailed above. The absorbance of TiO_2 has been calculated by subtracting the absorbance of the FTO substrate to the total absorbance of the FTO-TiO_2 sample.

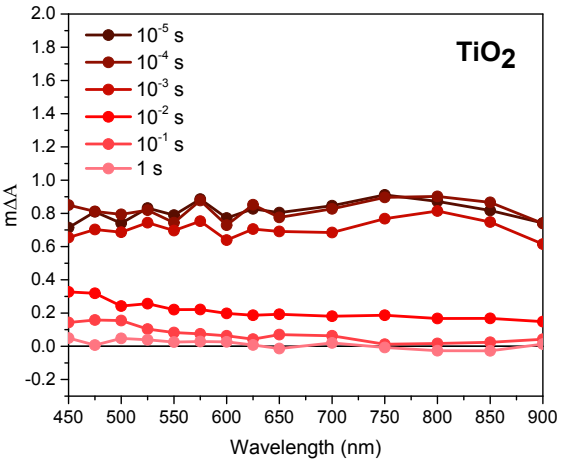

Figure S4. Transient absorption spectra of TiO_2 in ACN 0.1 M TEOA 0.1 M $TBAPF_6$ at high 355-nm excitation intensities (1.29±0.04 J/cm^2, 0.8 Hz) under −0.08 V *vs.* NHE.

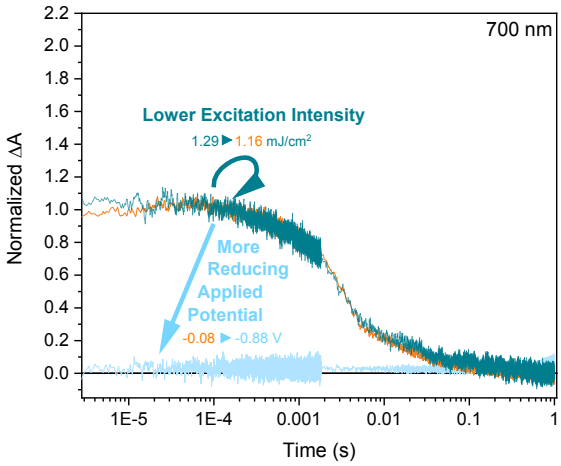

Figure S5. Dependency of charge accumulation kinetics in TiO_2 on bias and light intensity. The state represented in orange corresponds to a TiO_2 sample in ACN 0.1 M $TBAPF_6$ and 0.1 M TEOA under −0.08 V *vs.* NHE excited with a ~1.2 mJ/cm^2 355-nm laser pump (0.8 Hz repetition rate). As shown in the Figure, decreasing the excitation intensity in TiO_2 does not affect the electron signal decay (dark-blue to orange signal). Applying a potential of -0.88 V *vs.* NHE, in contrast, quenches the signal completely (pale-blue signal).

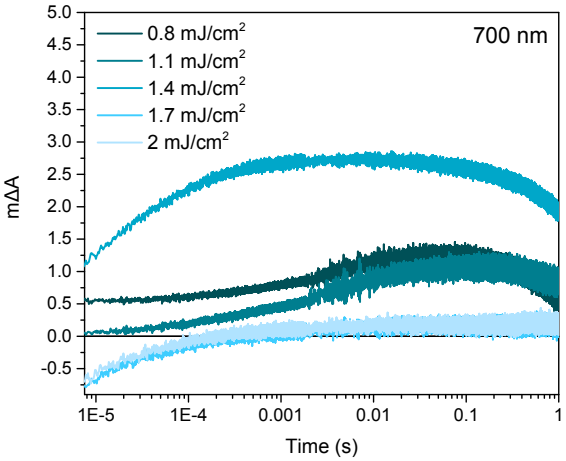

Figure S6. Kinetics at 700 nm of TiO_2-**CoP^2** in ACN 0.1 M $TBAPF_6$ with 0.1 M TEOA at different 355-nm excitation intensities (16 excitation shots averaged per measurement, 1 Hz) after 30 minutes in the dark. This figure shows the 700-nm kinetics of fresh samples, where the initial oxidation state of the catalyst is Co^{III}. Under 0.8, 1.1 and 1.4 excitation intensities, a positive signal corresponding to the Co(R)-to-Co(RR) reduction is observed, as assigned in the main text. Taking into account that each signal is the average of 16 laser pulses, this means that the photo-generated electrons reduce Co^{III} to Co(R), which accumulates between pulses, and Co(R) to Co(RR). At higher excitations intensities, however, the 700-nm signal changes radically. At high excitation intensities Co(R) is likely to be fully reduced to Co(RR) with the first laser pulse. Co(RR) persists in the dark until the next pulse comes and it reacts with photo-generated holes in the valence band. Because Co(RR) is the species in the sample with the highest extinction coefficient at 700 nm, the bleach at 700-nm is therefore due to the recombination of Co(RR) accumulated at the TiO_2 surface with valence band holes. These kinetic

changes cannot be due to catalyst degradation because the same amount of photons under −0.08 V *vs.* NHE bias leads to a much more robust signal at 700 nm (Figure 2A).

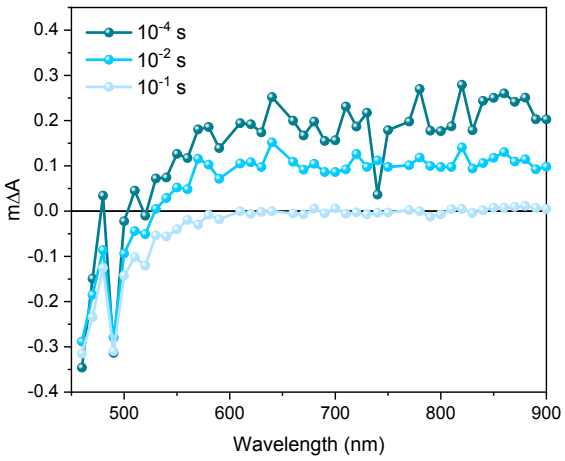

Figure S7. Transient absorption spectra of TiO_2-**CoP²** in ACN 0.1 M $TBAPF_6$ without TEOA after ~1.4 mJ/cm² 355-nm excitation, 0.8 Hz, at an applied potential of −0.08 V *vs.* NHE. In contrast to Figure S7B, with TEOA but without applied bias, the absence of TEOA under 0.2 V leads to a bleach peaking below 500 nm. As shown in Figure 3, Co(R) accumulates under −0.08 V *vs.* NHE and absorbs the strongest at ~470 nm in the 450-900 nm (Figure 2B). Therefore, the bleach at 450-500 nm is most likely due to the reaction of accumulated Co(R) with photo-generated holes.

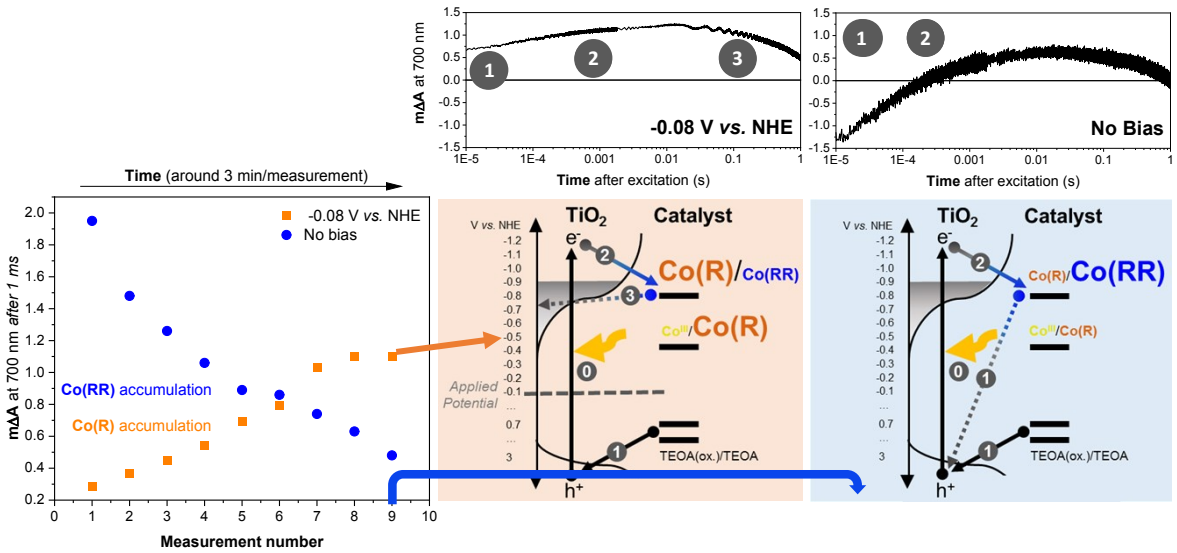

Figure S8. Illustration of the main accumulation and recombination processes observed in the data in Figure 4, where the kinetic traces shown here correspond to the *lightest-blue* kinetic signals with and without bias in Figure 4.

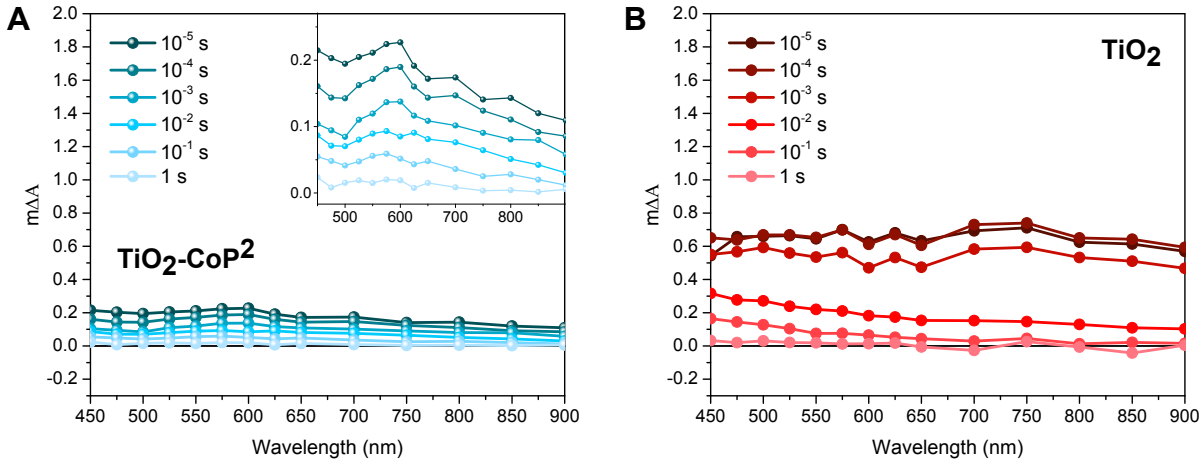

Figure S9. Transient absorption spectra of TiO_2-**CoP²** **(A)** and TiO_2 **(B)** in ACN 0.1 M TEOA 0.1 M $TBAPF_6$ at low 355-nm excitation intensities (1.16±0.03 J/cm², 0.8 Hz) under −0.08 V *vs.* NHE.

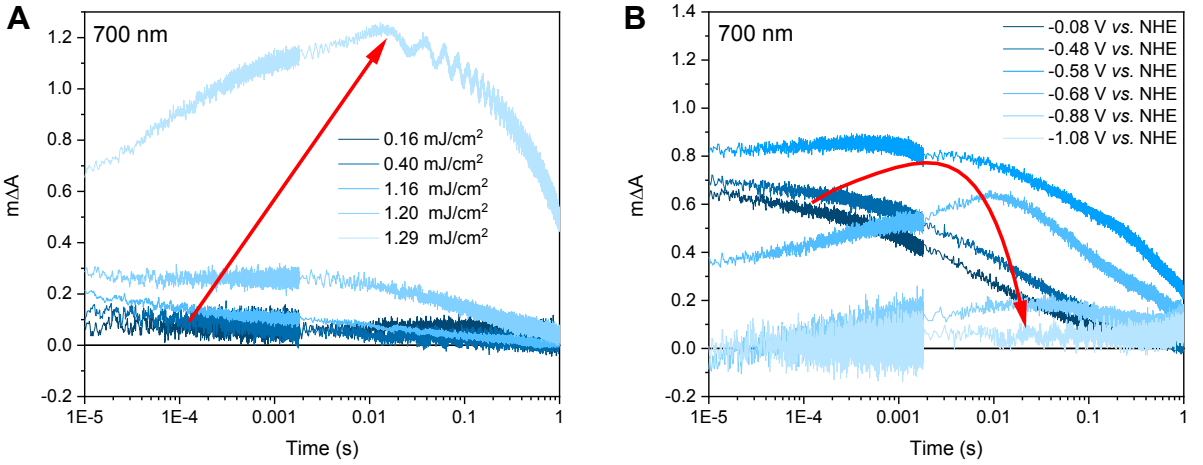

Figure S10. Dependency of the 700-nm kinetics in 2 different TiO_2-**CoP²** samples on **(A)** the excitation intensity (under −0.08 V vs NHE) and **(B)** the applied potential (with 1.16 mJ/cm² excitation). Repetition rate: 0.8 Hz.

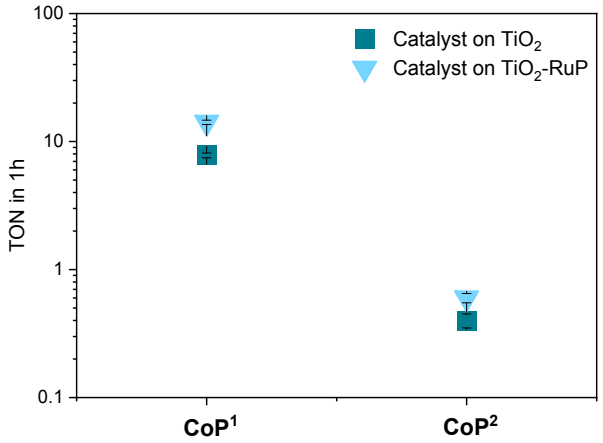

Figure S11. Hydrogen production of **CoP²** both on TiO_2 and TiO_2-RuP. To assess the catalytic activity of **CoP²** on TiO_2, we compare it to another catalyst immobilised on mesoporous TiO_2 films (i.e. **CoP¹**). The widely used cobaltoxime **CoP¹** has been taken as an indicator of the catalytic functionality of **CoP²** in conditions similar to the conditions reported in this work.[1-3] The H_2 production of TiO_2-**CoP¹** and TiO_2-**CoP²** was measured in the same conditions used in the rest of experiments reported here with 10% of water (ACN:H_2O 9:1, 0.1 M TEOA, 0.1 M $TBAPF_6$). The H_2 production of RuP-TiO_2-**CoP¹** and RuP-TiO_2-**CoP²** was taken from ref [3] (H_2O 0.1 M TEOA under AM 1.5G 100 mW/cm² irradiation, $\lambda > 422$ nm). We calculate the ratio of H_2 of the two catalysts in a given condition. Then, we compare the ratios in the two conditions (~20:1 **CoP¹**:**CoP²**).

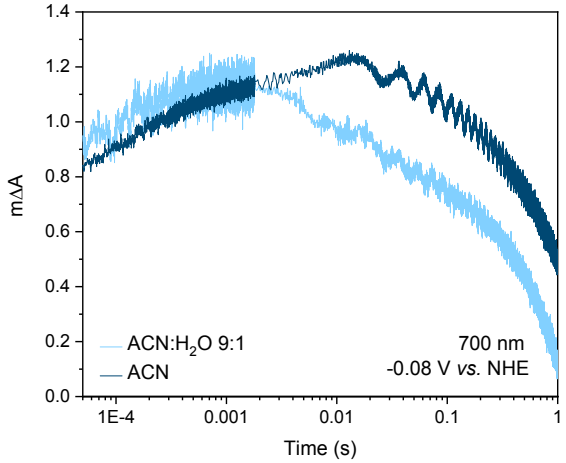

Figure S12. 700-nm kinetics of TiO_2-**CoP²** with and without 10% water (v/v) in acetonitrile with 0.1 M TEOA after ~1.4 mJ/cm² 355-nm excitation with 0.8 Hz laser repetition rate.

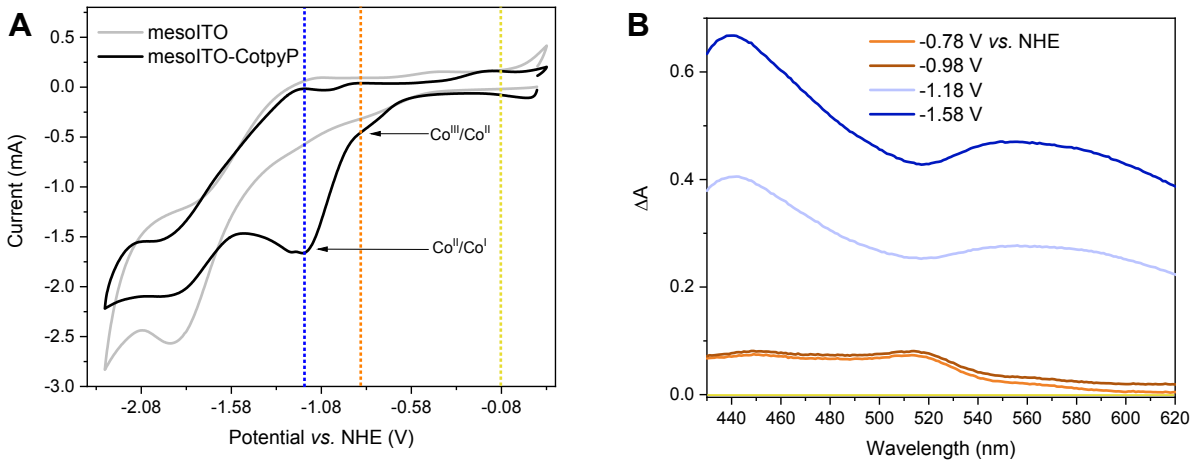

Figure S13. (A) Cyclic voltammetry of **CotpyP** on mesoITO. **(B)** Steady-state absorption difference of TiO_2-**CotpyP** under different applied potentials with respect to –0.08 V *vs*. NHE.

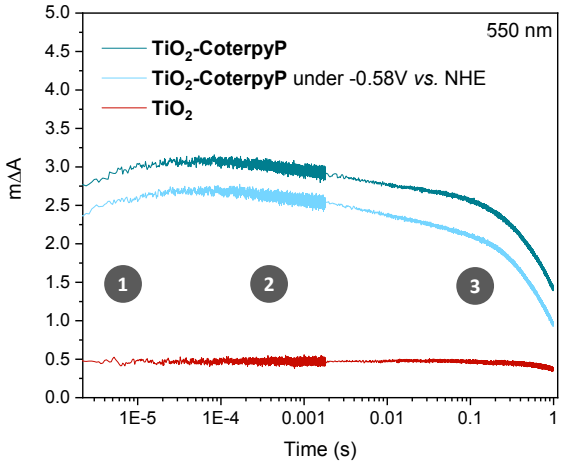

Figure S14. Absorption kinetics at 550 nm of TiO_2-**CotpyP** and TiO_2 in ACN 0.1 M $TBAPF_6$ 0.1 M TEOA after ~1.4 mJ/cm^2 355-nm excitation with 0.8 Hz laser repetition rate. The different processes taking place at different times (1-3) are illustrated in Figure S14.

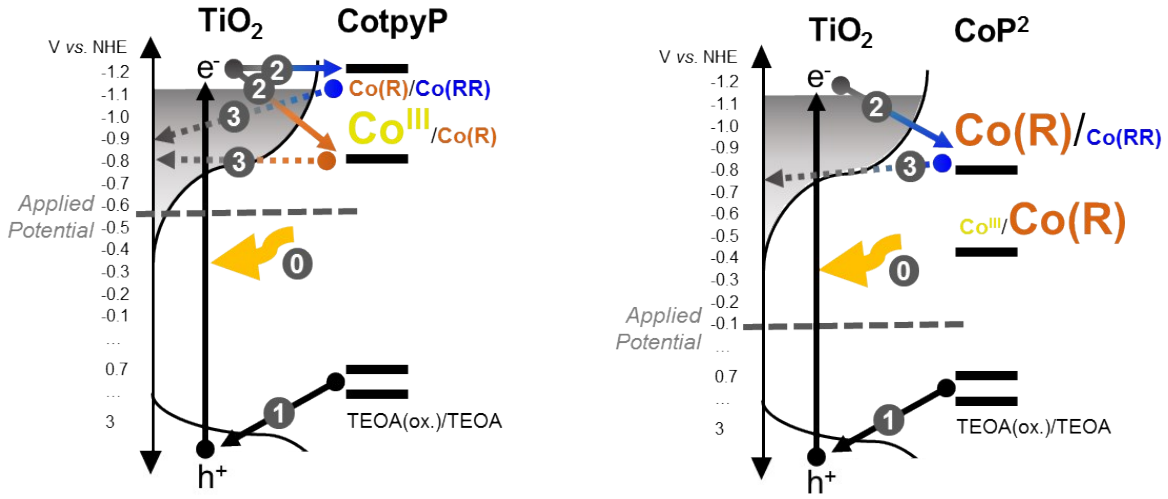

Figure S15. Illustration of the main electron transfer processes taking place in **(A)** TiO_2-**CotpyP** and **(B)** TiO^2-CoP^2 under intra-bandgap bias after exciting TiO_2 with high light intensities. The timescale of steps 1-3 is shown in Figures S13 and S8 respectively.

Table S1. UV/Vis Absorption maxima (UV/Vis transitions between 280-1000 nm) predicted by TD-DFT with B3LYP-def2tzvp (denoted B_def2tzvp), B3LYP-6-31G(d,p) (denoted B_6-31G**), TPSSh-def2tzvp (denoted T_def2tzvp) and TPSSh-6-31G(d,p) (denoted T_6-31G**) of the respective CoP^2 species (low-spin only, i.e. $M(Co^{II})=2$, $M(Co^{III})=1$). All transitions are given in nm.

	B_def2tzvp	B_6-31G**	T_def2tzvp	T_6-31G**
$[Co^{I}P^{2}]$	595	623	560	589
$[(Co^{II}P^{2})(MeCN)_2]^{+}$	339, 351	354, 364	374	386, 388
$[(Co^{III}P^{2})(MeCN)_2]^{2+}$	306, 319	297, 315	292, 327	298, 321
$[(Co^{III}P^{2})\ H]^{-}$	472	512	460	512

[($Co^{II}P^{2}$) H]$^{-}$	631, 674	613, 656	595, 604	605, 621

Table S2. Comparison of the Cobalt(III) coordination environment in the crystal structure of $[(Co^{III}P^2)(Br)_2]^4$ with the respective computed structures $[(Co^{III}P^2)(Br)_2]$ and $[(Co^{III}P^2)(MeCN)_2]^{2+}$ (low- and high-spin, i.e. **M(Co^{III})=1** and **M(Co^{III})=3**).

Parameter	**Experimental $[(Co^{III}P^2)(Br)_2]$**	**B_def2tzvp $[(Co^{III}P^2)(Br)_2]$**	**B_def2tzvp $[(Co^{III}P^2)(MeCN)_2]^{2+}$**	**B_6-31G** $[(Co^{III}P^2)(Br)_2]$**	**B_6-31G** $[(Co^{III}P^2)(MeCN)_2]^{2+}$**	**T_def2tzvp $[(Co^{III}P^2)(Br)_2]$**	**T_def2tzvp $[(Co^{III}P^2)(MeCN)_2]^{2+}$**	**T_6-31G** $[(Co^{III}P^2)(Br)_2]$**	**T_6-31G** $[(Co^{III}P^2)(MeCN)_2]^{2+}$**
Distances									
Co-N	1.91 1.91 1.90 1.90	1.95 1.91 1.91 1.92 1.92 1.94 1.92 1.95	1.96 1.94 1.93 1.93 1.92 1.94 1.96 1.96	1.94 1.91 1.91 1.90 1.92 1.92 1.94 1.93	1.95 1.93 1.92 1.93 1.95 1.95 1.93 1.92		1.95 1.93 1.92 1.92 1.94 1.95 1.90 1.92	1.93 1.90 1.91 1.89 1.93 1.92 1.90 1.90	1.91 1.94 1.91 1.91 1.93 1.91 1.93 1.90
Co-Br/ Co-N(MeCN)	2.75 2.99	2.43 2.45 2.68 2.64	1.89 1.89 2.19 2.17	2.40 2.39 2.62 2.61	1.88 1.88 2.14 2.15		1.87 1.87 2.14 2.14	2.37 2.36 2.58 2.58	1.85 1.85 2.10 2.12
C-C (eq)	1.51 1.48	1.48 1.46 1.47 1.45	1.46 1.48 1.45 1.48	1.48 1.46 1.47 1.45	1.48 1.46 1.48 1.46		1.47 1.46 1.47 1.44	1.47 1.45 1.46 1.44	1.46 1.47 1.47 1.45
Angle									
N-Co-N	82.8 80.5	82.1 80.8 82.0 80.6	82.1 80.8 82.2 80.5	82.1 80.9 82.1 80.7	82.4 81.1 82.3 80.8		82.3 81.0 80.7 82.3	82.19 81.13 82.07 80.88	81.4 82.4 82.3 81.1

UV/Vis spectra predicted by TD-DFT for the following different states:

Co1P2

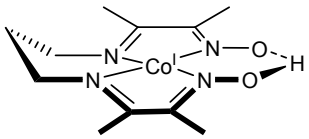

Co2P2_MeCN (for multiplicities 2 and 4 denoted by "[…]_2" and "[…]_4" respectively)

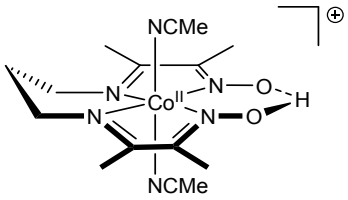

Co3P2_MeCN (for multiplicities 1 and 3 denoted by "[…]_1" and "[…]_3" respectively)

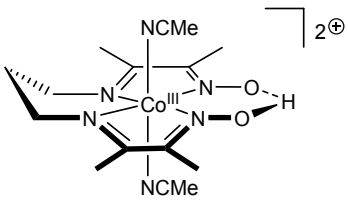

Co3P2_H (for multiplicities 1 and 3 denoted by "[…]_1" and "[…]_3" respectively)

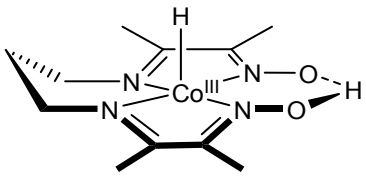

Co2P2_H (for multiplicities 2 and 4 denoted by "[…]_2" and "[…]_4" respectively)

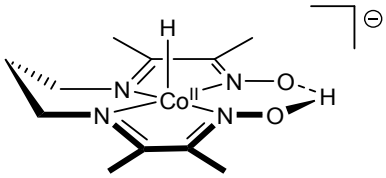

Co3P2_Br (for multiplicities 1 and 3 denoted by "[…]_1" and "[…]_3" respectively)

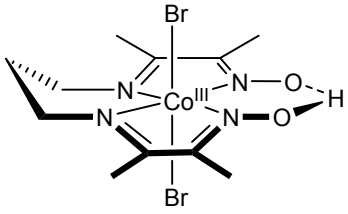

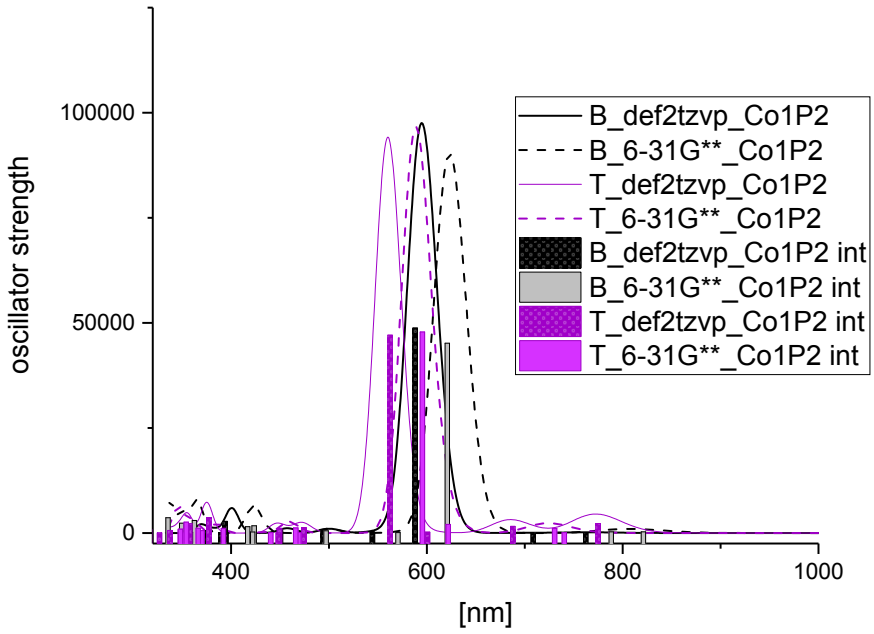
oscillator strength
100000
50000
0
400
600
800
1000
[nm]
B_def2tzvp_Co1P2
B_6-31G**_Co1P2
T_def2tzvp_Co1P2
T_6-31G**_Co1P2
B_def2tzvp_Co1P2 int
B_6-31G**_Co1P2 int
T_def2tzvp_Co1P2 int
T_6-31G**_Co1P2 int

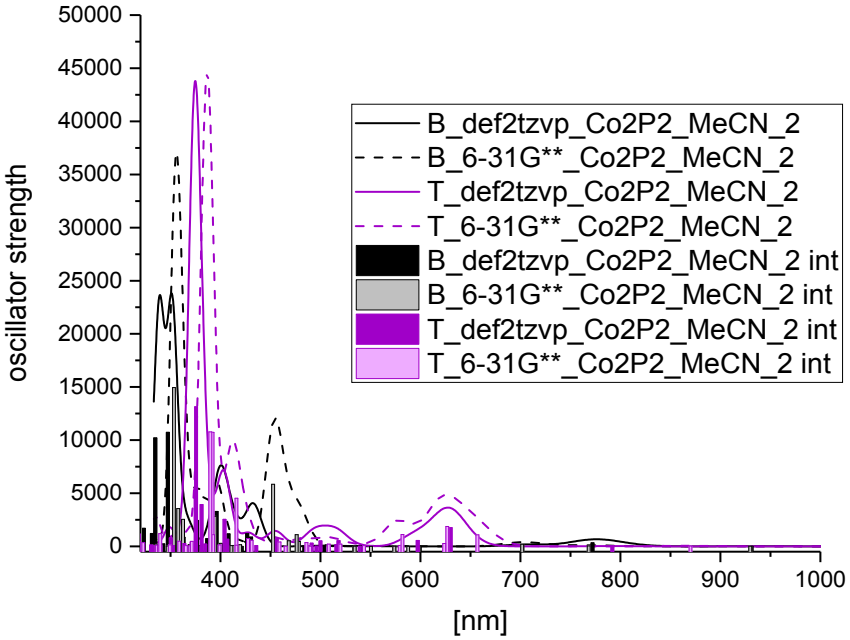
oscillator strength
50000
45000
40000
35000
30000
25000
20000
15000
10000
5000
0
400
500
600
700
800
900
1000
[nm]
B_def2tzvp_Co2P2_MeCN_2
B_6-31G**_Co2P2_MeCN_2
T_def2tzvp_Co2P2_MeCN_2
T_6-31G**_Co2P2_MeCN_2
B_def2tzvp_Co2P2_MeCN_2 int
B_6-31G**_Co2P2_MeCN_2 int
T_def2tzvp_Co2P2_MeCN_2 int
T_6-31G**_Co2P2_MeCN_2 int

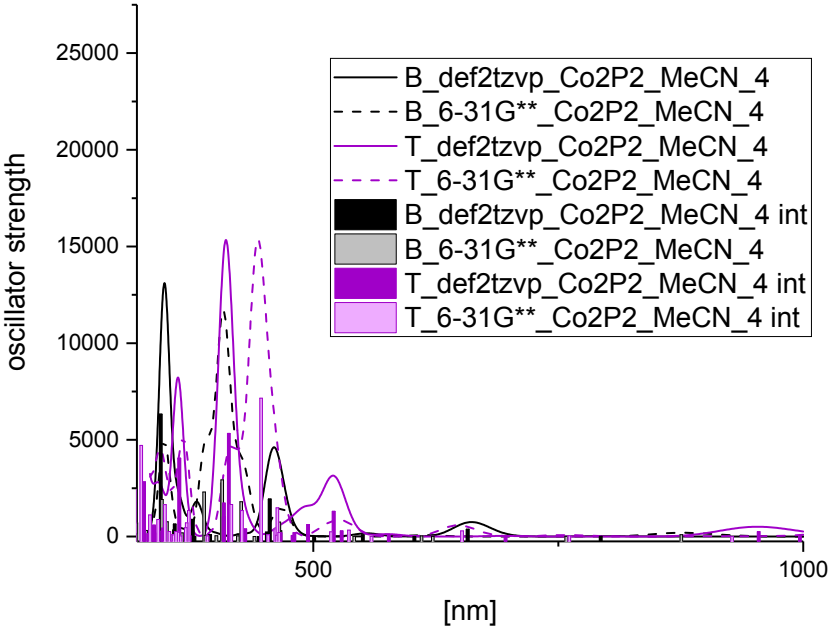
oscillator strength
25000
20000
15000
10000
5000
0
500
1000
[nm]
B_def2tzvp_Co2P2_MeCN_4
B_6-31G**_Co2P2_MeCN_4
T_def2tzvp_Co2P2_MeCN_4
T_6-31G**_Co2P2_MeCN_4
B_def2tzvp_Co2P2_MeCN_4 int
B_6-31G**_Co2P2_MeCN_4
T_def2tzvp_Co2P2_MeCN_4 int
T_6-31G**_Co2P2_MeCN_4 int

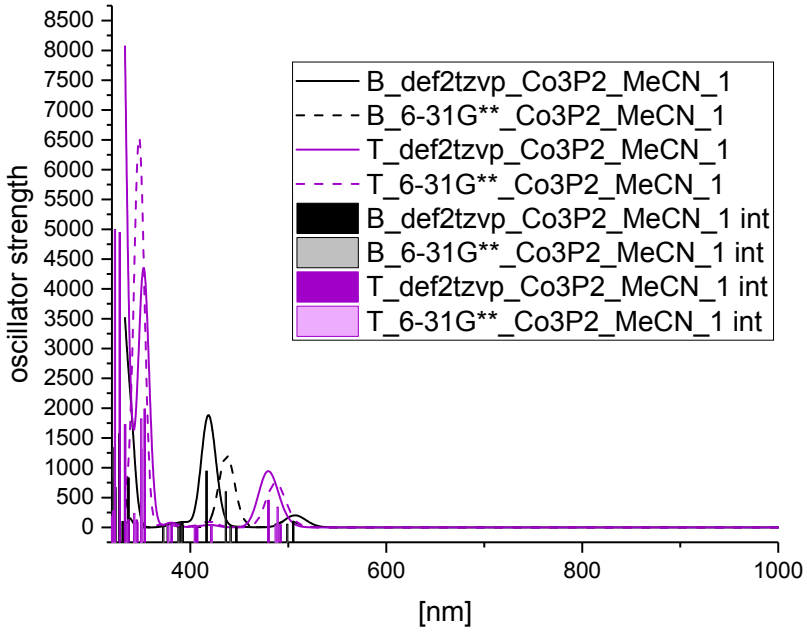
oscillator strength
8500
8000
7500
7000
6500
6000
5500
5000
4500
4000
3500
3000
2500
2000
1500
1000
500
0
400
600
800
1000
[nm]
B_def2tzvp_Co3P2_MeCN_1
B_6-31G**_Co3P2_MeCN_1
T_def2tzvp_Co3P2_MeCN_1
T_6-31G**_Co3P2_MeCN_1
B_def2tzvp_Co3P2_MeCN_1 int
B_6-31G**_Co3P2_MeCN_1 int
T_def2tzvp_Co3P2_MeCN_1 int
T_6-31G**_Co3P2_MeCN_1 int

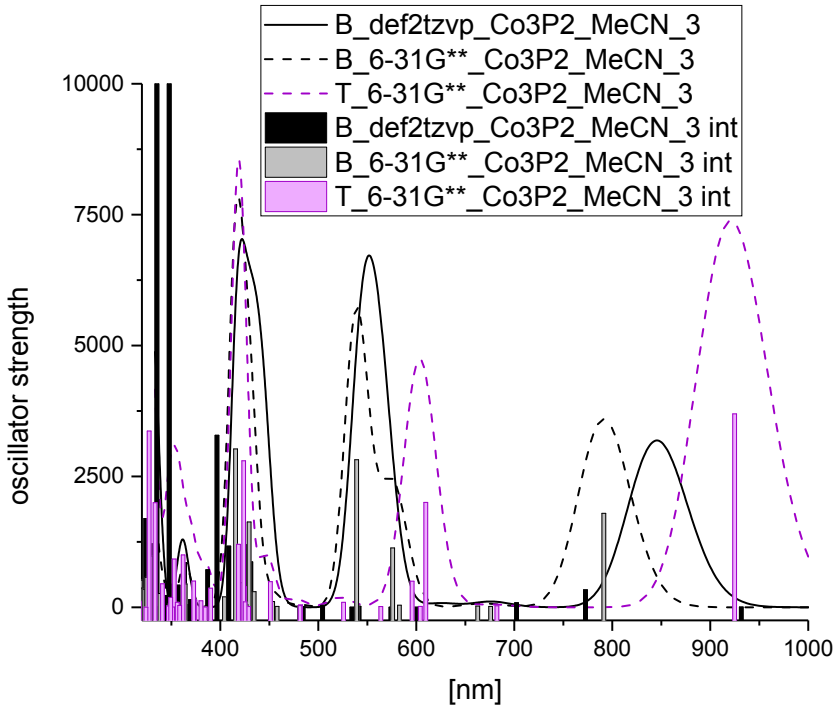
B_def2tzvp_Co3P2_MeCN_3
B_6-31G**_Co3P2_MeCN_3
T_6-31G**_Co3P2_MeCN_3
B_def2tzvp_Co3P2_MeCN_3 int
B_6-31G**_Co3P2_MeCN_3 int
T_6-31G**_Co3P2_MeCN_3 int
oscillator strength
[nm]

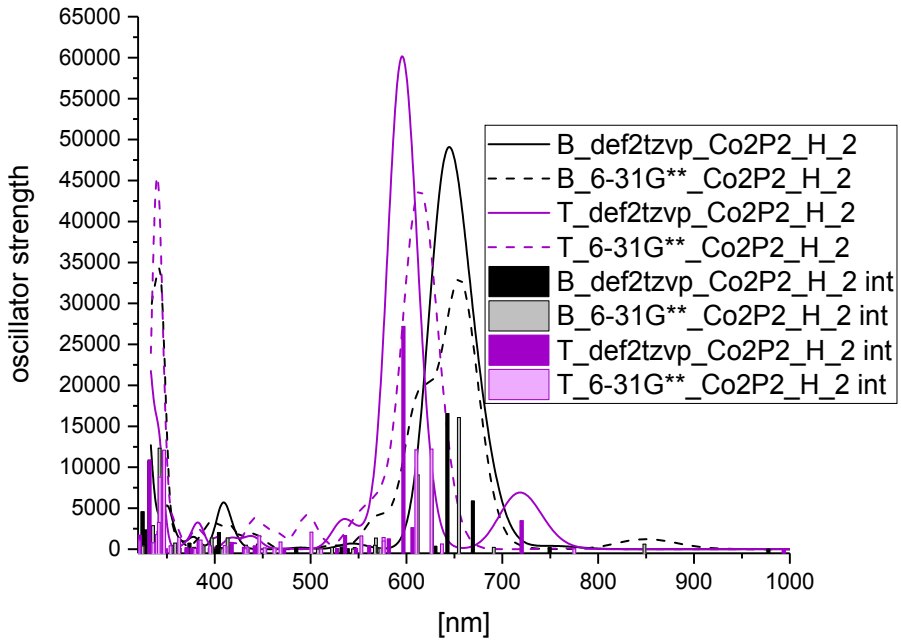
B_def2tzvp_Co2P2_H_2
B_6-31G**_Co2P2_H_2
T_def2tzvp_Co2P2_H_2
T_6-31G**_Co2P2_H_2
B_def2tzvp_Co2P2_H_2 int
B_6-31G**_Co2P2_H_2 int
T_def2tzvp_Co2P2_H_2 int
T_6-31G**_Co2P2_H_2 int
oscillator strength
[nm]

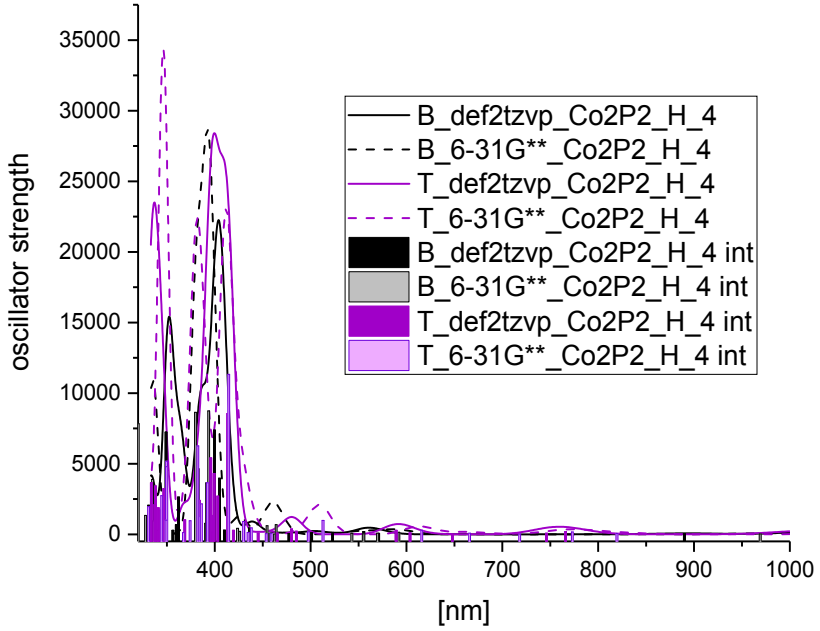
oscillator strength
35000
30000
25000
20000
15000
10000
5000
0
400
500
600
700
800
900
1000
[nm]
B_def2tzvp_Co2P2_H_4
B_6-31G**_Co2P2_H_4
T_def2tzvp_Co2P2_H_4
T_6-31G**_Co2P2_H_4
B_def2tzvp_Co2P2_H_4 int
B_6-31G**_Co2P2_H_4 int
T_def2tzvp_Co2P2_H_4 int
T_6-31G**_Co2P2_H_4 int

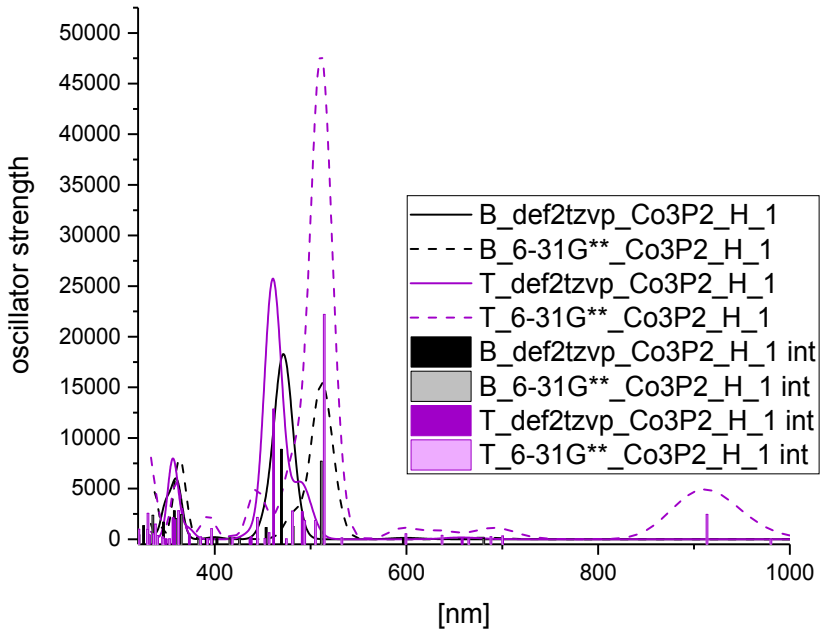
oscillator strength
50000
45000
40000
35000
30000
25000
20000
15000
10000
5000
0
400
600
800
1000
[nm]
B_def2tzvp_Co3P2_H_1
B_6-31G**_Co3P2_H_1
T_def2tzvp_Co3P2_H_1
T_6-31G**_Co3P2_H_1
B_def2tzvp_Co3P2_H_1 int
B_6-31G**_Co3P2_H_1 int
T_def2tzvp_Co3P2_H_1 int
T_6-31G**_Co3P2_H_1 int

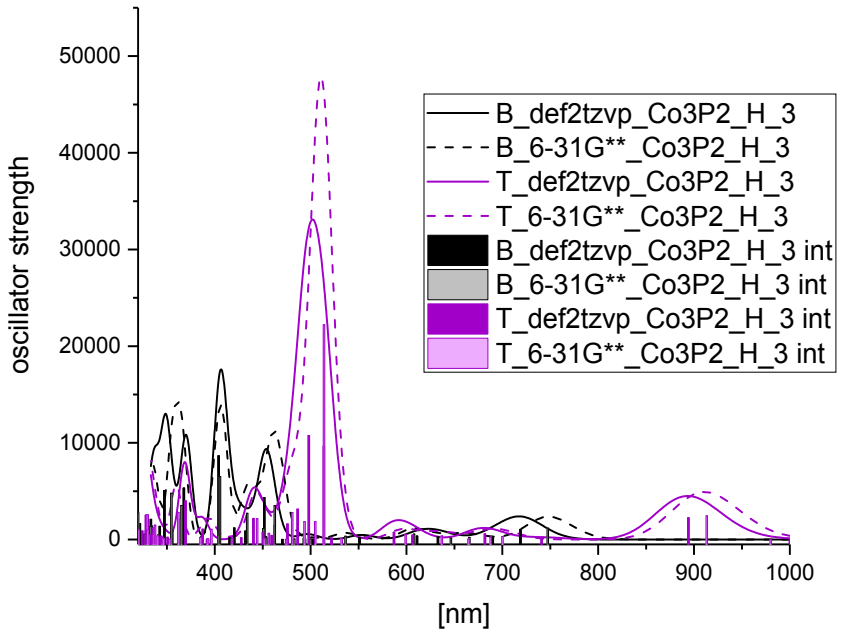
oscillator strength
50000
40000
30000
20000
10000
0
400
500
600
700
800
900
1000
[nm]
B_def2tzvp_Co3P2_H_3
B_6-31G**_Co3P2_H_3
T_def2tzvp_Co3P2_H_3
T_6-31G**_Co3P2_H_3
B_def2tzvp_Co3P2_H_3 int
B_6-31G**_Co3P2_H_3 int
T_def2tzvp_Co3P2_H_3 int
T_6-31G**_Co3P2_H_3 int

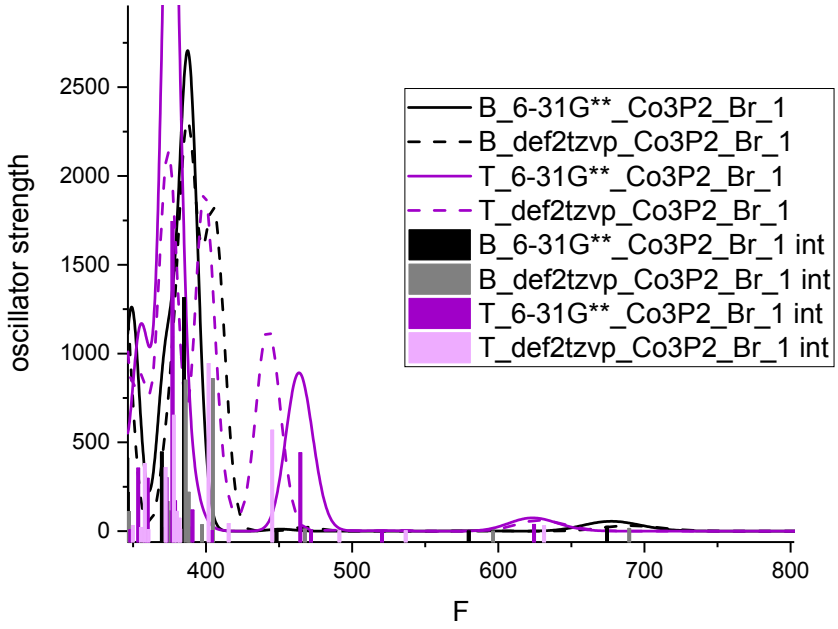
oscillator strength
2500
2000
1500
1000
500
0
400
500
600
700
800
F
B_6-31G**_Co3P2_Br_1
B_def2tzvp_Co3P2_Br_1
T_6-31G**_Co3P2_Br_1
T_def2tzvp_Co3P2_Br_1
B_6-31G**_Co3P2_Br_1 int
B_def2tzvp_Co3P2_Br_1 int
T_6-31G**_Co3P2_Br_1 int
T_def2tzvp_Co3P2_Br_1 int

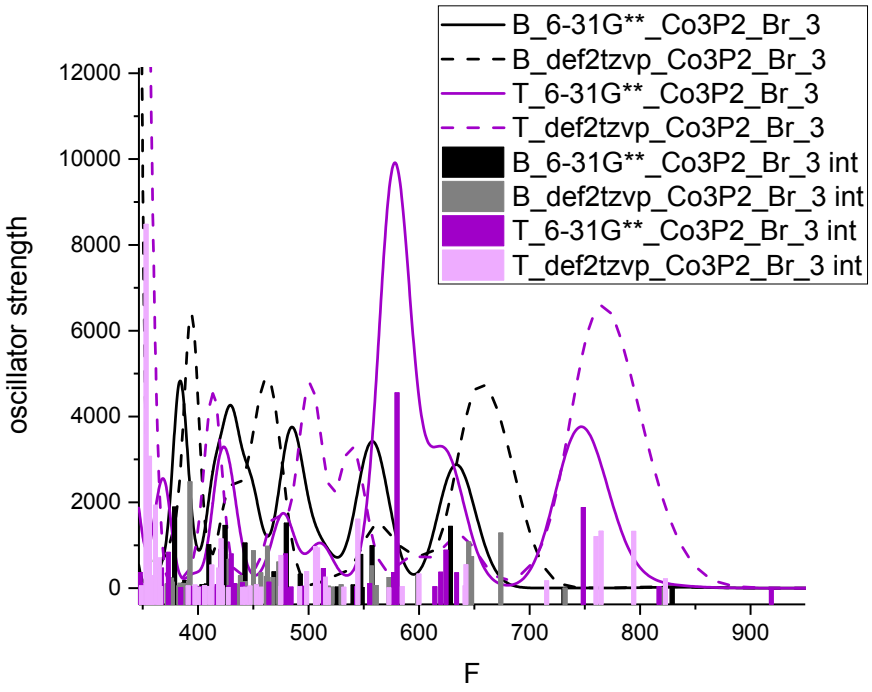
B_6-31G**_Co3P2_Br_3
B_def2tzvp_Co3P2_Br_3
T_6-31G**_Co3P2_Br_3
T_def2tzvp_Co3P2_Br_3
B_6-31G**_Co3P2_Br_3 int
B_def2tzvp_Co3P2_Br_3 int
T_6-31G**_Co3P2_Br_3 int
T_def2tzvp_Co3P2_Br_3 int
oscillator strength
12000
10000
8000
6000
4000
2000
0
400
500
600
700
800
900
F

References

1. F. Lakadamyali, A. Reynal, M. Kato, J. R. Durrant and E. Reisner, *Chem Eur J*, 2012, **18**, 15464-15475.
2. F. Lakadamyali and E. Reisner, *Chem Commun (Camb)*, 2011, **47**, 1695-1697.
3. J. Willkomm, N. M. Muresan and E. Reisner, *Chem Sci*, 2015, **6**, 2727-2736.
4. N. M. Muresan, J. Willkomm, D. Mersch, Y. Vaynzof and E. Reisner, *Angew Chem Int Ed Engl*, 2012, **51**, 12749-12753.
5. J. J. Leung, J. Warnan, K. H. Ly, N. Heidary, D. H. Nam, M. F. Kuehnel and E. Reisner, *Nature Catalysis*, 2019, **2**, 354-365.
6. J. J. Leung, J. A. Vigil, J. Warnan, E. Edwardes Moore and E. Reisner, *Angew Chem Int Ed Engl*, 2019, **58**, 7697-7701.
7. X. Li, *Imperial College London*, 2012.
8. S. Ito, T. N. Murakami, P. Comte, P. Liska, C. Grätzel, M. K. Nazeeruddin and M. Grätzel, *Thin Solid Films*, 2008, **516**, 4613-4619.
9. C. J. Barbé, F. Arendse, P. Comte, M. Jirousek, F. Lenzmann, V. Shklover and M. Grätzel, *J. Am. Ceram. Soc*, 1997, **80**, 3157–3171.
10. J. N. Clifford, E. Palomares, M. K. Nazeeruddin, R. Thampi, M. Grätzel and J. R. Durrant, *J. Am. Chem. Soc.*, 2004, **126**, 5670-5671.
11. E. S. Rountree, B. D. McCarthy, T. T. Eisenhart and J. L. Dempsey, *Inorg Chem*, 2014, **53**, 9983-10002.
12. E. M. Espinoza, J. A. Clark, J. Soliman, J. B. Derr, M. Morales and V. I. Vullev, *Journal of The Electrochemical Society*, 2019, **166**, H3175-H3187.
13. V. V. Pavlishchuk and A. W. Addison, *Inorganica Chimica Acta* 2000, **298**, 97–102.
14. C. Lee, W. Yang and R. G. Parr, *Phys Rev B Condens Matter*, 1988, **37**, 785-789.
15. A. D. Becke, *Physical Review A*, 1988, **38**, 3098-3100.
16. A. D. Becke, *The Journal of Chemical Physics*, 1993, **98**, 5648-5652.
17. P. A. M. Dirac, *Proc Royal Soc A*, 1929, **123**, 714-733.
18. J. C. Slater, *Physical Review*, 1951, **81**, 385-390.
19. J. P. Perdew and Y. Wang, *Phys Rev B Condens Matter*, 1992, **45**, 13244-13249.
20. J. Tao, J. P. Perdew, V. N. Staroverov and G. E. Scuseria, *Phys Rev Lett*, 2003, **91**, 146401.
21. V. N. Staroverov, G. E. Scuseria, J. Tao and J. P. Perdew, *J Chem Phys*, 2003, **119**, 12129.
22. F. Weigend and R. Ahlrichs, *Phys Chem Chem Phys*, 2005, **7**, 3297-3305.
23. F. Weigend, *Phys Chem Chem Phys*, 2006, **8**, 1057-1065.
24. W. J. Hehre, R. Ditchfield and J. A. Pople, *The Journal of Chemical Physics*, 1972, **56**, 2257-2261.
25. M. M. Francl, W. J. Pietro, W. J. Hehre, J. S. Binkley, M. S. Gordon, D. J. DeFrees and J. A. Pople, *J Chem Phys*, 1982, **77**, 3654.
26. V. A. Rassolov, J. A. Pople, M. A. Ratner and T. L. Windus, *The Journal of Chemical Physics*, 1998, **109**, 1223-1229.
27. F. Neese, *Wiley Interdisciplinary Reviews: Computational Molecular Science*, 2012, **2**, 73-78.
28. S. Sinnecker, A. Rajendran, A. Klamt, M. Diedenhofen and F. Neese, *J Phys Chem A*, 2006, **110**, 2235-2245.
29. S. Grimme, J. Antony, S. Ehrlich and H. Krieg, *J Chem Phys*, 2010, **132**, 154104.
30. S. Grimme, S. Ehrlich and L. Goerigk, *J Comput Chem*, 2011, **32**, 1456-1465.
31. M. D. Hanwell, D. E. Curtis, D. C. Lonie, T. Vandermeersch, E. Zurek and G. R. Hutchison, *Journal of Cheminformatics*, 2012, **4**.